Further improvement and analysis of CCD scheme: Dissipation discretization and de-aliasing properties

T.K. Sengupta *, V.V.S.N. Vijay, S. Bhaumik

Department of Aerospace Engineering, I.I.T. Kanpur, U.P. 208016, India

A R T I C L E   I N F O

A B S T R A C T

In this paper, we further analyze a combined compact difference (CCD) scheme proposed recently [T.K. Sengupta, V. Lakshmanan, V.V.S.N. Vijay, A new combined stable and dispersion relation preserving compact scheme for non-periodic problems, J. Comput. Phys. 228 (8) (2009) 3048–3071] for its dissipation discretization properties to show that its superiority also helps in controlling aliasing error for a benchmark internal flow. However, application of the same CCD method to study the receptivity of a boundary layer experiencing adverse pressure gradient is not successful. This is traced to the nature of the equilibrium flow where the better dissipation property is not helpful in the inviscid part of the flow, where the aliasing problems continue to persist. A further modification is proposed to the CCD method here to solve complex physical problems requiring information on higher order disturbance quantities – as in problems of flow receptivity and instability.

1. Introduction

Combined compact difference (CCD) schemes are very high accuracy methods where first and second derivatives are evaluated simultaneously, from implicit relations between the dependent variable and its derivatives obtained using Hermitian polynomials [1–4]. This method belongs to the family of compact schemes and hence affords near-spectral accuracy in solving convection–diffusion dominated flows, as noted in [5–8]. In [5], methods are indicated to obtain first and second derivatives separately by using compact schemes. CCD schemes [2–4,8] provide second derivatives simultaneously, that makes computations faster, increasing the efficiency via enhanced resolution of dissipation terms for convection–diffusion dominated problems. This makes the method very attractive, however only when one works in the physical plane with uniform grids.

In all the presented results here, we have used the four-stage fourth-order accurate Runge–Kutta method for time advancement as defined and analyzed in [7,11]. The analysis of compact schemes for first derivatives has attracted a lot of attention in [6,7,9,10] to investigate wave propagation problems. Such analyses indicate the suitability of the method for solving convection dominated problems. In [11], a comprehensive analysis is made to understand what constitutes error in a signal propagation problem establishing the correct error analysis, as opposed to the existing von Neumann analysis. The application of this analysis technique for solving uni- and bi-directional wave problems was also provided in [4], while investigating an improved CCD scheme. The same scheme is analyzed and compared with other methods for their dissipation discretization and de-aliasing properties. In this method [4], not only the dispersion relation preservation (DRP) property is

imp... ...od eli...
the ... ...ation
As a ...Navier...
pres... ...s num...
linea... ...ity as...
high... ...ue for
accu... ...forms...
sion... ...– as h...
tane... ...ropert...
repr... ...m int...
A... ...ting th...
sch... ...ge, thi...
gul... ...ity usi...
pea... ...lution...
bec... ...ts [12,
me... ...s can b...
er... ...ion, di...
ha... ...g flow...
tv... ...ors no...
p... ...e to sh...
w... ...cally fo...
t... ...t to rig...
p... ...ortex s...
g... ...l triang...
t... ...one al...
... ...3) tho...
...d num...
...nely hi...
...le sho...
...mpreh...
...terms...
...uate fi...
...differe...
...super...
...in ter...
...arison...
...avier–S...

0.8

S1

S3

C2

C1

Aliasing errors are made whenever products of two or more space dependent functions are computed. This does not have to occur due to nonlinearity of the problem [14]. For example in [14], the source of aliasing was traced to the discretization of dissipation terms in the transformed plane. However, in the present exercise we compute the Navier–Stokes equation in the physical plane using uniform grids. For such a case, the only source of aliasing is due to the nonlinear convection terms. The topic of aliasing error has received attention due to its importance in computing different fluid flows and other problems of mathematical physics [15–19]. In [15,18], aliasing is proposed to be controlled by reformulating the governing equations. General discussion on aliasing in computations are available in [14,16,17] with respect to finite difference methods using non-uniform grids. Specific post-processing methods to control aliasing are given in [14,16,19]. It is noted that aliasing problem leads to numerical instability specifically for high wave number components.

For the square lid-driven cavity problem, aliasing increases with Reynolds number. For example, for $Re \geqslant Re_{crit}$, the flow becomes time-dependent and one requires good DRP property to capture the correct space-time dependence. Additionally, with increase in Re, newer length scales appear in the form of smaller vortices forming inside the cavity. The corner vortices [20] clearly show the presence of newer scales, specifically near the top right corner and these created high wave numbers cause aliasing. This increase of band-width of the energy spectrum requires increased resolution of the numerical method. If the grid resolution is not increased proportionately with Re, convection terms produce aliasing leading to accumulation of energy at high wave numbers. Left uncontrolled, this energy pile-up leads to numerical instability. This is a major source of error and should be avoided at all costs. Bruneau and Saad [21] have used (1024×1024) grid to obtain solution for $Re = 10,000$, while using CD_2 scheme in discretizing diffusion terms and third order upwind scheme for convection terms. The CD_2 for the dissipation terms attenuates it appreciably, making the equivalent Re higher than the actual value. At the same time, use of higher order upwind schemes compensate this loss of physical dissipation at the higher wave numbers. Use of staggered grid also helps to remove aliasing error [14]. Use of staggered grid with low order method is based on the similar work reported in [22]. In [23], a seventh order upwind scheme was used to discretize the convection terms and a sixth order central difference method to discretize diffusion terms on a collocated grid for the lid-driven cavity flow problem.

There are just the opposite effects on aliasing by lower and higher accuracy methods for the discretization of convection and diffusion terms. Discretization of convection terms by lower accuracy methods severely attenuates the unknown at higher wave numbers reducing the effect of aliasing. In contrast, high accuracy methods do not filter at moderate length scales and are prone to display aliasing if adequate resolution is not used. For dissipation terms, lower accuracy methods have lower effective dissipation, which is equivalent to increasing Re that will excite more spatial scales increasing the possibility of aliasing. For high accuracy methods, the dissipation terms are properly resolved [4] preventing formation of spurious additional scales that can add to aliasing. For the CCD method in [4], the evaluated second derivatives have more than adequate dissipation across all wave numbers. Here we explore the consequence of this property of the CCD method [4], whether this can be effectively used to alleviate the problem of aliasing in comparison to other high accuracy methods. We also test this for both internal and external flows and if necessary, propose further improvements to the CCD method [4].

The paper is formatted in the following manner. In the next section, we describe briefly the CCD scheme and provide various performance parameters for the diffusion terms along with a discussion on effectiveness of dissipation discretization. In Section 3, results for the square lid-driven cavity problem are discussed with respect to aliasing effects and its control for internal flows. In Section 4, receptivity of boundary layer experiencing adverse pressure gradient to time-harmonic excitations is studied. Such excitations create instability waves and makes a good test case for external flows. Finally, a summary and conclusion is provided in Section 5.

2. Combined compact difference scheme for non-periodic problem

Let us consider a domain with $(N + 1)$ equidistant points with spacing Δx where a function u is defined. The CCD scheme is used to simultaneously evaluate the first and second derivatives (u'_j, u''_j) from the following discrete equations for interior nodes, in terms of the function (u_j) values [2,8],

$$\frac{7}{16}(u'_{j+1} + u'_{j-1}) + u'_j - \frac{\Delta x}{16}(u''_{j+1} - u''_{j-1}) = \frac{15}{16\Delta x}(u_{j+1} - u_{j-1}) \tag{1}$$

$$\frac{9}{8\Delta x}(u'_{j+1} - u'_{j-1}) - \frac{1}{8}(u''_{j+1} + u''_{j-1}) + u''_j = \frac{3}{\Delta x^2}(u_{j+1} - 2u_j + u_{j-1}) \tag{2}$$

Eq. (1) is used for $j = 3$ to $(N - 1)$, while Eq. (2) is used for $j = 2$ to $j = N$. If we consider Dirichlet boundary conditions at $j = 1$ and $(N + 1)$, then there are $(2N + 2)$ unknown derivatives, with four unknowns provided at the nodes, $j = 1$ and $(N + 1)$ for the derivatives. These boundary derivatives are used as: at $j = 1 : u'_1 = (-1.5u_1 + 2u_2 - 0.5u_3)/\Delta x$ and $u''_1 = (u_1 - 2u_2 + u_3)/(\Delta x)^2$. At $j = (N + 1)$, we have used similar expression for $u''_{(N+1)}$, while for $u'_{(N+1)}$ the expression on the right hand side has signs reversed. We however, note that in solving Navier–Stokes equation we do not need the derivatives at the boundaries, where only the Dirichlet conditions on ψ are used. Wall vorticity is calculated from the kinematic definition of it from the stream function equation.

A full-domain analysis method [6] applied on the CCD scheme of [2] for the one dimensional convection problem shows it to be numerically unstable near the inflow boundary. Similar instability near inflow boundary was diagnosed earlier for

many compact schemes and new boundary stencils were proposed to rectify this instability problem in [6]. Hence, for the CCD scheme [2] we have used similar boundary stencils, and the analysis in [4] show that this rectified and controlled near-boundary instability. Additional two equations to complete the system are given by,

$$u'_2 = \frac{1}{\Delta x}\left[\left(\frac{2\beta_2}{3}-\frac{1}{3}\right)u_1 - \left(\frac{8\beta_2}{3}+\frac{1}{2}\right)u_2 + (4\beta_2+1)u_3 - \left(\frac{8\beta_2}{3}+\frac{1}{6}\right)u_4 + \frac{2\beta_2}{3}u_5\right] \tag{3}$$

$$u'_N = -\frac{1}{\Delta x}\left[\left(\frac{2\beta_N}{3}-\frac{1}{3}\right)u_{N+1} - \left(\frac{8\beta_N}{3}+\frac{1}{2}\right)u_N + (4\beta_N+1)u_{N-1} - \left(\frac{8\beta_N}{3}+\frac{1}{6}\right)u_{N-2} + \frac{2\beta_N}{3}u_{N-3}\right] \tag{4}$$

with $\beta_2 = -0.025$ and $\beta_N = 0.09$. These constants for Eqs. (3) and (4) were optimized for the OUCS3 scheme defined in [6,14] for the first derivative and they have been adopted here as they are.

The multiplicative constants in Eqs. (1) and (2) for the interior stencils are fixed by matching coefficients of Taylor series expansion up to the sixth order. Thus, we have a complete linear algebraic system for the evaluation of first and second derivatives as defined later in Eq. (10). In the present work, we highlight only essential steps and leave out the intermediate steps for the readers to refer to [4,11] where a complete analysis has been provided for the discretization method and associated error evolution equation.

Exact spatial first derivative of u is given by, $\left[\frac{\partial u}{\partial x}\right]_{exact} = \int ikUe^{ikx}dk$ where k denotes the wave number in the spectral plane. Discrete computing methods obtain this first spatial derivative u' as,

$$\left[u'_j\right]_{numerical} = \int ik_{eq}Ue^{ikx_j}dk \tag{5}$$

with different methods having different expressions for k_{eq}. The quantity $\frac{k_{eq}}{k}$ is in general complex, with the real part representing the numerical method's ability to resolve various scales in the spectrum and the imaginary part indicates added numerical dissipation, when it is negative. One can adopt the same procedure in expressing the second spatial derivative in the spectral plane in a non-dimensional form, with the real part of $-\frac{k_{eq}^{(2)}}{k^2}$ representing scale-wise dissipation and the imaginary part representing added numerical dispersion. We can also write the CCD stencils given by Eqs. (1)–(4) as linear algebraic equations given by,

$$[A_1]\{u'\} + [B_1]\{u''\} = [C_1]\{u\} \tag{6}$$
$$[A_2]\{u'\} + [B_2]\{u''\} = [C_2]\{u\} \tag{7}$$

On solving these two simultaneous equations we arrive at,

$$\{u'\} = \frac{1}{\Delta x}[D_1]\{u\} \tag{8}$$

$$\{u''\} = \frac{1}{\Delta x^2}[D_2]\{u\} \tag{9}$$

where,

$$[D_1] = ([A_1] - [B_1][B_2]^{-1}[A_2])^{-1}([C_1] - [B_1][B_2]^{-1}[C_2])$$
$$[D_2] = ([B_2] - [A_2][A_1]^{-1}[B_1])^{-1}([C_2] - [A_2][A_1]^{-1}[C_1])$$

Thus, $\frac{k_{eq}}{k}$ and $\frac{k_{eq}^{(2)}}{k^2}$ for different nodes for first and second derivatives are evaluated from Eqs. (8) and (9) as,

$$\left(\frac{k_{eq}}{k}\right)_j = \frac{1}{k\Delta x}\sum_{l=1}^{N+1}(D_1)_{jl}(P)_{lj}$$

$$\left(\frac{k_{eq}^{(2)}}{k^2}\right)_j = \frac{1}{(k\Delta x)^2}\sum_{l=1}^{N+1}(D_2)_{jl}(P)_{lj}$$

where j defines the node number and $(P)_{lj} = e^{i(l-j)k\Delta x}$ is the element of the projection matrix that helps defining the derivatives locally, so that a comparison is possible directly with spectral method.

However, while implementing the above mentioned CCD scheme to obtain simultaneously the first and second derivatives for solving governing differential equations, we recommend not to follow the matrix inversion method as indicated above that involves large computations. The above expressions are used for analysis only. Instead, it is advised to use the Block Tridiagonal Matrix Algorithm (Block TDMA), [25] to reduce computational time and improve efficiency of solution process. The necessary framework of the structure of the scheme to obtain derivatives efficiently is demonstrated below. We rewrite the CCD stencils given by Eqs. (1)–(4) as,

$$[A]\{du\} = \{B\} \tag{10}$$

where the matrix $[A]$ can be expanded as,

$$[A] = \begin{pmatrix} [Q]_1 & [R]_1 & \cdots & \cdots & \cdots & \cdots & \cdots & \cdots & \cdots & 0 \\ [P]_2 & [Q]_2 & [R]_2 & & & & & & & \vdots \\ \vdots & [P]_3 & [Q]_3 & [R]_3 & & & & & & \vdots \\ \vdots & & \ddots & \ddots & \ddots & & & & & \vdots \\ \vdots & & & [P]_{i-1} & [Q]_{i-1} & [R]_{i-1} & & & & \vdots \\ \vdots & & & & [P]_i & [Q]_i & [R]_i & & & \vdots \\ \vdots & & & & & \ddots & \ddots & \ddots & & \vdots \\ \vdots & & & & & & [P]_{N-1} & [Q]_{N-1} & [R]_{N-1} & 0 \\ \vdots & & & & & & & [P]_N & [Q]_N & [R]_N \\ 0 & \cdots & \cdots & \cdots & \cdots & \cdots & \cdots & 0 & [P]_{N+1} & [Q]_{N+1} \end{pmatrix}$$

and the unknown $\{du\}$ vector can be written as,

$$\{du\} = \{\, du_1 \quad du_2 \quad du_3 \quad \ldots \quad du_{i-1} \quad du_i \quad du_{i+1} \quad \ldots \quad du_{N-1} \quad du_N \quad du_{N+1} \,\}^T$$

and likewise vector $\{B\}$ can be written as,

$$\{B\} = \{\, b_1 \quad b_2 \quad b_3 \quad \ldots \quad b_{i-1} \quad b_i \quad b_{i+1} \quad \ldots \quad b_{N-1} \quad b_N \quad b_{N+1} \,\}^T$$

Thus, the i-th nodal equation for the above system, $[A]\{du\} = \{B\}$ is given by,

$$[P]_i\{du\}_{i-1} + [Q]_i\{du\}_i + [R]_i\{du\}_{i+1} = \{b\}_i \tag{11}$$

It is noted that each individual element of matrix $[A]$ is a (2×2) block matrix and $\{du\}$ and $\{B\}$ are (2×1) vectors. For the interior stencils, along the i-th row of $[A]$, elements of (11) can be written as,

$$[P]_i = \begin{bmatrix} \frac{7}{16} & \frac{\Delta x}{16} \\ -\frac{9}{8\Delta x} & -\frac{1}{8} \end{bmatrix}$$

$$[Q]_i = \begin{bmatrix} 1 & 0 \\ 0 & 1 \end{bmatrix}$$

$$[R]_i = \begin{bmatrix} \frac{7}{16} & -\frac{\Delta x}{16} \\ \frac{9}{8\Delta x} & -\frac{1}{8} \end{bmatrix}$$

These expressions of the block matrices hold for interior nodes only. Elements along the i-th row of vectors $\{du\}$ and $\{B\}$ are given by,

$$\{du\}_i = \begin{Bmatrix} u'_i \\ u''_i \end{Bmatrix}$$

$$\{b\}_i = \begin{Bmatrix} \frac{15}{16\Delta x}\left(u_{j+1} - u_{j-1}\right) \\ \frac{3}{\Delta x^2}\left(u_{j+1} - 2u_j + u_{j+1}\right) \end{Bmatrix}$$

In the same way, one can also represent the boundary stencil given in Eqs. (3) and (4) to form the modified (2×2) block matrices at $j = 2$ and N to form a complete system. Note that the solution of Eq. (10) will provide the first and second derivative from $j = 1$ to $(N + 1)$. Thus for a non-periodic problem, with Dirichlet boundary conditions provided at $j = 1$ and $j = (N + 1)$, one would use the computed derivatives from Eq. (10) from $j = 2$ to N only.

To quantify effectiveness of dissipation discretization terms by any numerical method, we define an equivalent gain function $GF(k)$ as,

$$GF(k) = -\left(\frac{k^{(2)}_{eq}}{k^2}\right)_{real} \tag{12}$$

where the subscript *real* indicates the real part of the complex quantity $-\frac{k^{(2)}_{eq}}{k^2}$.

Ideally, the numerical method should have the right hand side of Eq. (12) as unity over the entire range of resolved wave numbers, i.e., the Nyquist limit. However, any discrete computing method does not satisfy this requirement uniformly all the way up to the Nyquist limit. This departure from ideal value represents the loss of effectiveness of the dissipation discretization with respect to the corresponding spectral representation. Thus, we define a function $LF(k)$ as,

$$LF(k) = 1 - GF(k) \tag{13}$$

that provides the relative loss of physical dissipation due to discretization as a function of wave number.

In Fig. 2a, $GF(k)$ is plotted against $k\Delta x$ at different nodes for different discrete schemes, comprising the CD_2; the CD_4 explicit schemes; the compact scheme of Lele for second derivative [5] and the CCD scheme represented by Eqs. (1)–(4). Here, we considered a domain of 31 points for the analysis. The explicit schemes' properties are same at all nodes, while the properties of implicit schemes are node-dependent. Moreover for the implicit schemes, properties at most of the interior nodes are same, with significant departures noted for the near-boundary points. It is for these reasons we have shown only some typical nodal properties near the center and one of the boundaries in Figs. 2a and 2b. Near the inflow ($j = 2$ and 3), original CCD scheme [2] introduces *anti-diffusion* while obtaining the first derivative and this was rectified by using Eqs. (3) and (4) for boundary closure in [4]. It is obvious that the CD_2 scheme acts as a very low-pass filter and the figure shows serious loss of dissipation at all wave numbers except a very small range near the origin. However, it is noted that unlike the case of first spatial derivative (where the equivalent wave number drops to zero at the Nyquist limit), the quantity $\left(-\frac{k_{eq}^{(2)}}{k^2}\right)_{real}$ has a value of $\frac{4}{\pi^2}$ for the CD_2 scheme at $k\Delta x = \pi$. For DNS, the Nyquist limit corresponds to *the Kolmogorov* scale where kinetic energy is converted into heat by the action of molecular viscosity. Thus, an inferior resolution of dissipation at this scale severely compromises the ability for DNS. It is clear that the CD_4 scheme is superior to CD_2 scheme across all length scales. Specifically, there is significant improvement of 38%, at the smallest length scale ($k\Delta x = \pi$), while for the intermediate $k\Delta x$ ranges, there is uniform benefit. It is seen that there is no loss of physical dissipation up to $k\Delta x = 1.0$ for the CD_4 scheme, a similar feature was noted while discretizing convection terms by the fourth-order accurate central difference formula [14]. The high reso-
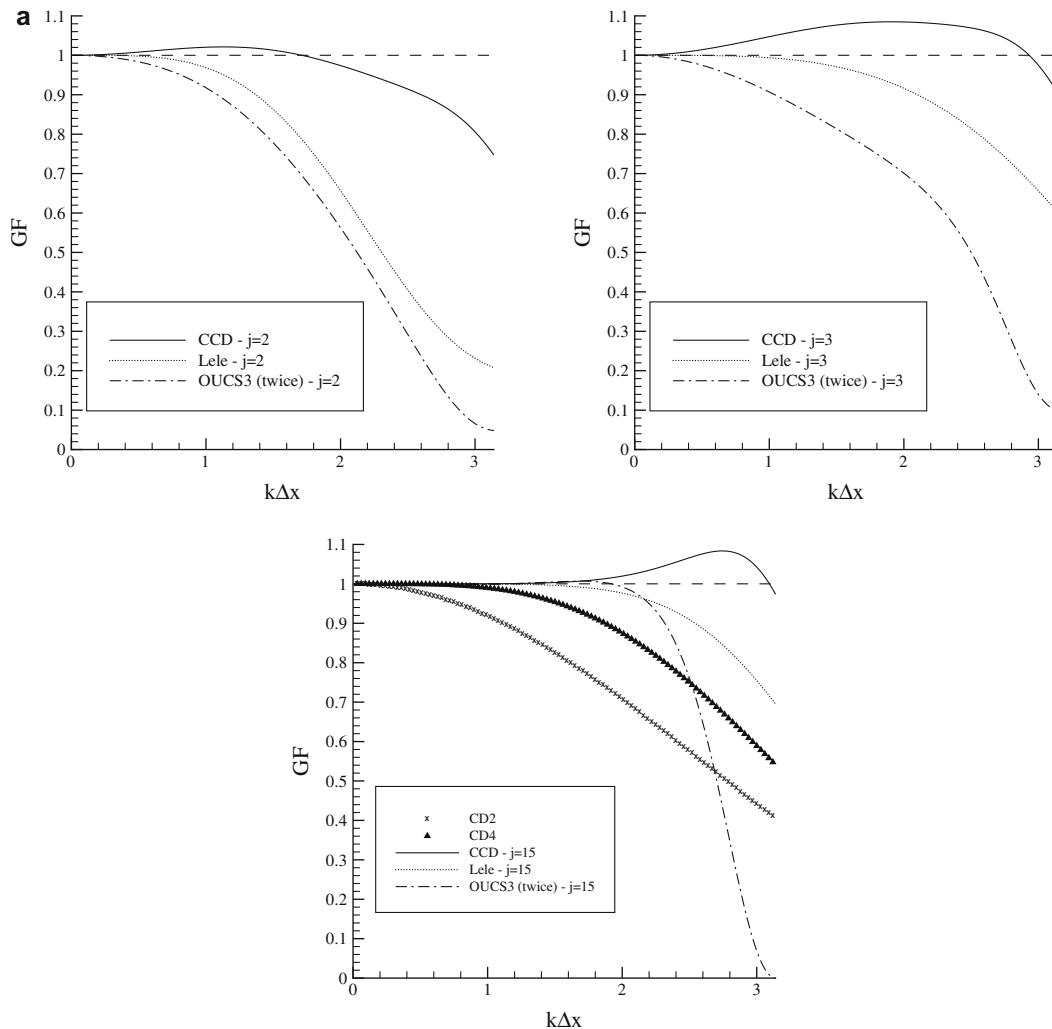

Fig. 2a. The gain function, $GF(k) = \left\{\frac{-k_{eq}}{k^2}\right\}$ is plotted against $k\Delta x$ for different schemes at near-boundary ($j = 2\&3$) and inner stencil ($j = 15$) points for different schemes. Explicit second and fourth-order schemes ($CD_2\&CD_4$) are inferior to Lele's compact scheme [5] and CCD scheme [4]. OUCS3 scheme [6] for first derivative has been applied twice to obtain the second derivative. The dashed line in each frame indicates the ideal value of $GF(k) = 1$.
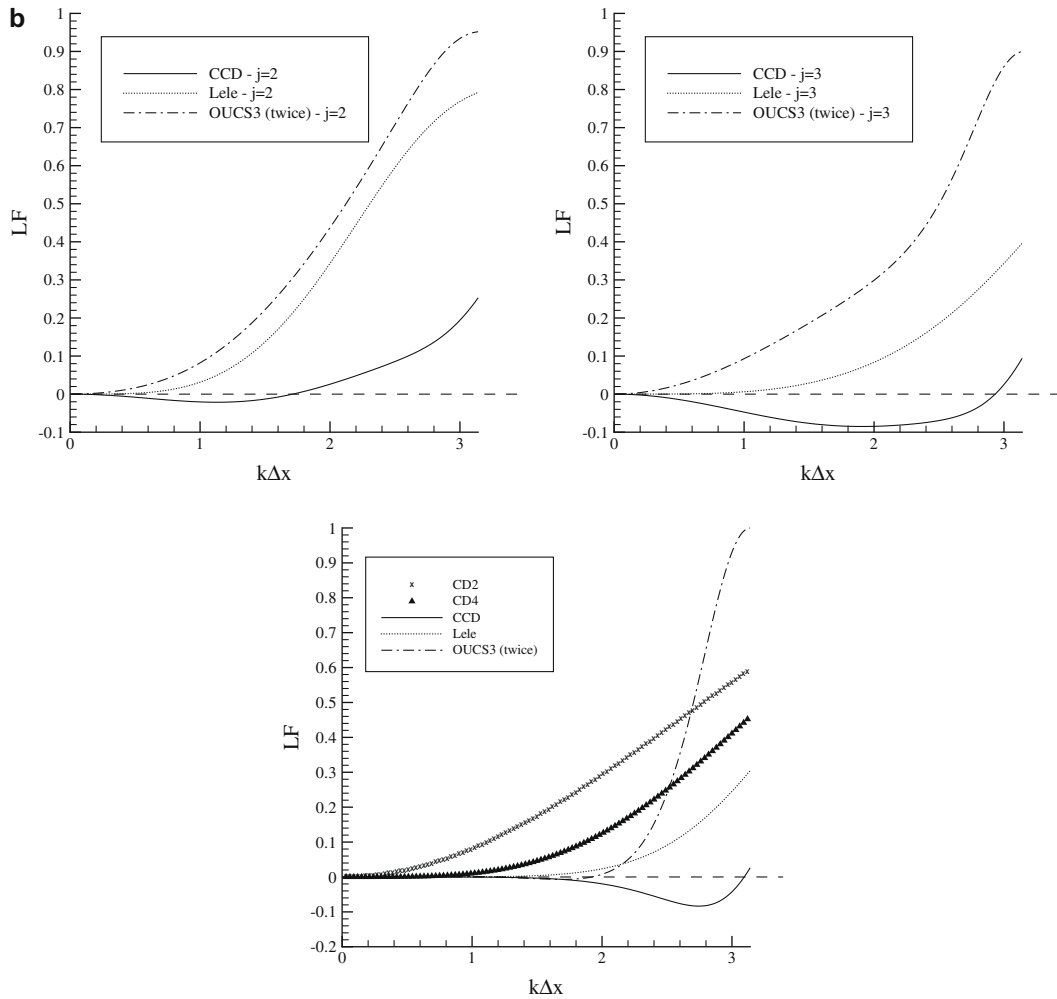
Fig. 2b. The loss function, $LF(k) = (1 - GF(k))$ is plotted against $k\Delta x$ for different schemes shown in Fig. 2a. The dashed line in each frame indicates the ideal value of $LF(k) = 0$.

lution of compact schemes for first derivatives also extend to the second derivatives- noted for interior, as well as the near-boundary points in Fig. 2a. In the figure, $GF(k)$ for the compact scheme of [5] is found to be superior than the CD_2 and the CD_4 schemes. For this scheme at the interior of the domain, effectiveness of physical dissipation is preserved till $k\Delta x = 1.5$ and there is 75% improvement in physical dissipation representation at the Nyquist limit as compared to the CD_2 scheme. The effectiveness of CCD scheme [4] is seen to be the best among all these methods, as there is no loss of physical dissipation up to a $k\Delta x$ range that is much higher than the method in [5]. Moreover, there is an overshoot at higher wave numbers indicating additional dissipation that can actually work as an advantage for the method, which is explained as a way to control aliasing. We have already noted that a second derivative can be obtained by using the method to calculate first derivative twice in succession. However, the effectiveness of calculating the first derivative is always reduced to zero at the Nyquist limit and thus calculating second derivative by applying a method of calculating first derivative twice was considered inferior. But, Fig. 2a shows the curious feature of OUCS3 method when applied twice to obtain the second derivative, to have better discretization property than the compact method of [5] up to a larger range of $k\Delta x$ – as seen for interior nodes. This is however, not the case for the near-boundary points. The second derivative can be obtained in the interior of the domain without any loss, up to $k\Delta x = 1.92$ by the OUCS3 method, as compared to [5] providing a 25% improvement. This benefit of OUCS3 method can be further extended to higher wave numbers by judicious use of upwinding while evaluating convection terms and this is described later. The OUCS3 method is not superior to the methods of calculating second derivatives directly [5] for the near-boundary points ($j = 2, 3$).

Next, one would like to quantify the loss of physical dissipation as a function of k. In Fig. 2b, $LF(k)$ vs. $k\Delta x$ is shown for all these schemes at different nodes. In this figure, severe loss of physical dissipation incurred by the explicit central differencing methods over a large band of length scales is evident. This is lesser for the Lele's scheme for the interior nodes only. One can notice further improvement when OUCS3 scheme is used twice to obtain the second derivative for the interior nodes.
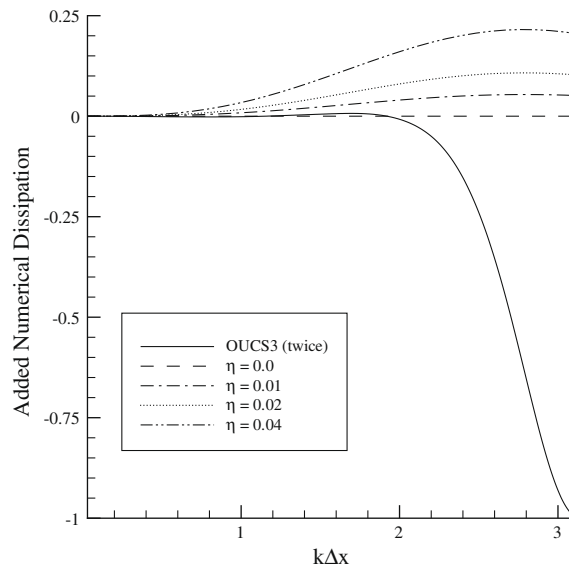
Fig. 3. The loss function for the OUCS3 scheme applied twice to obtain second derivative is shown with solid line and added numerical dissipation by OUCS3 scheme while discretizing the convection terms is also shown as a function of wave number for different values of the upwinding constant η.

The CCD scheme shows no loss of dissipation for all k. Instead, it adds extra dissipation at wave numbers given by $k\Delta x \geqslant 1.8$ and this helps to reduce aliasing error at higher k. We have noted that energy piles up at higher k due to aliasing and excess dissipation of CCD scheme can effectively remove this at every step of the computation. This is demonstrated by solving Navier–Stokes equation in the next section.

Next, we show how OUCS3 scheme for second derivative can be used effectively to compute Navier–Stokes equation by a judicious mix of upwinding the corresponding convection term. In Fig. 3, the loss function of OUCS3 method in calculating the second derivative is shown by a solid line. A negative value in the figure implies a loss of dissipation and the figure shows that it starts affecting the calculations at $k\Delta x = 1.92$. However, in an actual calculation where the convection terms are also evaluated by OUCS3 scheme, the overall method can retain its accuracy up to a higher value of $k\Delta x$. Since the OUCS3 method for the first derivative is an upwind scheme, one actually adds implicitly some dissipation via the higher order dissipation term of the form $\eta \Delta x^3 \frac{\partial^4 u}{\partial x^4}$. By a proper choice of η, one can add numerical dissipation via this term at high k only, where the loss of physical dissipation is noted. In Fig. 3, added dissipation is shown along the positive ordinate for different values of η that can counteract the loss of physical dissipation of the OUCS3 method shown along the negative ordinate. In the convection terms of Navier–Stokes equation, local velocity components appear multiplied with the numerical dissipation term and thus no general prescription can be provided to counteract the loss of physical dissipation. However, the literature is replete with evidences by various efforts where upwinding has been noted as an effective procedure to produce accurate solution, specially in performing LES [26]. This is also essentially the basis for performing monotone implicit large eddy simulations (MILES). Additional dissipation enforced at higher wave numbers not only regains the loss of physical dissipation but also provides a means to control the aliasing error which is mostly dominant at higher k.

We re-iterate that the CCD scheme has the unique property among the compact schemes that the physical dissipation is represented exactly at low- to mid-range of k, while it provides additional dissipation at higher k to provide additional mechanism to control aliasing at higher k. Thus, the combined effect of high resolution for the first derivatives in CCD [4], and adequate representation of physical dissipation without any loss, coupled with the additional degree of freedom in controlling aliasing error makes it an excellent method for high accuracy simulation. To show this, we present the solution of 2D Navier–Stokes equation by solving (a) the square lid-driven cavity problem for $Re = 10,000$ and (b) the receptivity calculation of a boundary layer experiencing adverse pressure gradient with respect to a localized time-harmonic excitation. For such unsteady internal and external flows, large range of k are excited those contribute to aliasing arising solely from the convection terms.

3. Two-dimensional square lid-driven cavity problem

The flow in a square lid-driven cavity (LDC) constitutes a classical benchmark problem, due to its unique boundary conditions that allow comparison of any new method's potential in solving Navier–Stokes equation. Here, the two-dimensional incompressible, viscous flow is solved in stream function-vorticity formulation given in non-dimensional form by,

$$\frac{\partial^2 \psi}{\partial x^2} + \frac{\partial^2 \psi}{\partial y^2} = -\omega \tag{14}$$

$$\frac{\partial \omega}{\partial t} + u \frac{\partial \omega}{\partial x} + v \frac{\partial \omega}{\partial y} = \frac{1}{Re} \left(\frac{\partial^2 \omega}{\partial x^2} + \frac{\partial^2 \omega}{\partial y^2} \right) \tag{15}$$

$$u = \frac{\partial \psi}{\partial y} \tag{16}$$

$$v = -\frac{\partial \psi}{\partial x} \tag{17}$$

where ω is the only non-zero component of vorticity vector normal to the plane of the flow; ψ represents the stream function and (u, v) are the Cartesian components of the velocity in the x- and y-directions, respectively. The $(\psi - \omega)$ formulation is suitable due to various reasons. The primary reason is for checking CCD, that requires working in a collocated uniform grid. One can use primitive variable formulation, but for numerical reasons one needs to either work on a staggered grid (as in [22]) or use an upwind scheme in a collocated grid. Present CCD method uses a central scheme and is suited for working on non-staggered grid. This formulation is also known for its inherent accuracy and computational efficiency in satisfying mass conservation exactly over the full domain. As we intend to use the present CCD scheme for solving Eqs. (14)–(17), we have used a uniform grid with (256×256) points for simulating the flow at $Re = 10,000$. To solve Eq. (14), we have used the Bi-CGSTAB method- a fast and convergent elliptic pde solver [24]. Residual convergence criteria for Eq. (14) is taken as 10^{-6} and the CCD scheme is used also to discretize second derivatives of ψ. In obtaining the first and second derivatives for Eqs. (14) and (15) by CCD method, we have used the Block Tridiagonal matrix algorithm (Block TDMA) [25] to reduce the number of computations otherwise involved in obtaining and evaluating the inverse of the matrices D_1 and D_2 for solving Eqs. (8) and (9).

Results for this flow obtained by the CCD method are compared with the solution obtained by using a different method of discretization. In this alternate method, we used the OUCS3 scheme [6,14] for discretizing the convection terms and the Lele's scheme [5] for discretizing the diffusion terms. We call this alternate as the OUCS3-Lele method here. To test aliasing and stability properties of this alternate method, we first solved Eqs. (14)–(17) using the CCD method to obtain the solution for which the transients have decayed. This "equilibrium solution" obtained at $t = 300$ is already shown in Fig. 1. We have used this as the initial solution for further simulation by the OUCS3–Lele method. Lack of effective dissipation discretization of this method has the twin effects of (i) causing the numerical simulation to be for an effectively higher Reynolds number flow and (ii) being unable to control aliasing at high k. In the vorticity contours of Fig. 1, one can clearly see minor grid scale oscillations under the lid on top right corner.

In the computed solution with the CCD scheme, one notes multi-periodic nature of the vorticity field with time. The multiplicity of the time scales is due to different vortical structures noted in different part of the cavity in Fig. 1, with different topology and dynamics with well defined time period. We note that the solution obtained by CCD scheme provides an altogether new intermediate solution. In this solution, a triangular vortex is noted at the center of the cavity, surrounded by three gyrating vortices as satellites. Existence of triangular vortex has been reported earlier in [12,13] for different rotational flows both experimentally and numerically- but in both these cases triangular vortex was found to be transient in nature in the experiment. Flows were simulated using discrete vortex models in these references- and not by solving full Navier–Stokes equation. We attribute the success of the CCD method to the proper resolution of dissipation terms and an effective coupling between the discretization of convection and diffusion terms in combination. Computed vortical structures are found to be multi-periodic, stable and self-sustaining over a long period of time, once the triangular vortex has been formed. Vorticity contours obtained by the CCD method are shown in Fig. 4 for various non-dimensional times up to $t = 580$; the computations have been performed even longer that show the triangular vortex to persist. The evolution of the weak triangular vortex is caused by the gyration of the outer layer of rotating fluid, that in turn has been caused by the constant lid motion. From $t = 300$ to $t = 400$, the triangular vortex shrinks from its full size, as it becomes weaker and weaker. Subsequently, the vortex grows again fed by another layer of fluid from the outer rotating layer. The continuous supply of energy provided by the driven lid enables the cyclic variations seen for the triangular core.

In Fig. 5, vorticity contours obtained using OUCS3–Lele method are compared with the results from the CCD method. It is seen that the two solutions match overall- as noted up to $t = 340$. Same contour levels are shown in all the frames of Figs. 4 and 5 for an effective comparison. The phase and dispersion properties of any two methods differ and that is responsible for the mismatch seen here. Some high k oscillations are noted in Figs. 4 and 5, on the top right hand corner due to aliasing, that is more for the OUCS3–Lele method. Both the methods have similar propagation property (as shown in [4]), it is the lesser effectiveness of dissipation discretization of OUCS3–Lele method at higher k that is responsible for higher aliasing. Despite the simple geometry and unambiguous boundary conditions, this flow is complex. The flow remains confined, but the energy is continuously fed through the lid motion. Existence of strict multi-periodicity indicates a steady state, that is achieved by accurate discretization method ensuring proper resolution of convection and diffusion terms in providing neutral numerical stability. It would be shown in Fig. 6, that there are also qualitative differences between these two methods at subsequent times. However, both the methods do not suffer excessively from the effects of aliasing to cause numerical instability i.e. the aliasing error is not cumulative in this case.

In Fig. 6, we have shown the vorticity time histories of the obtained solutions at fixed location $(0.95, 0.95)$ in the cavity using CCD (top-left) and OUCS3–Lele methods (top-right) to show multiple time-periodic solution at this Re that agrees well
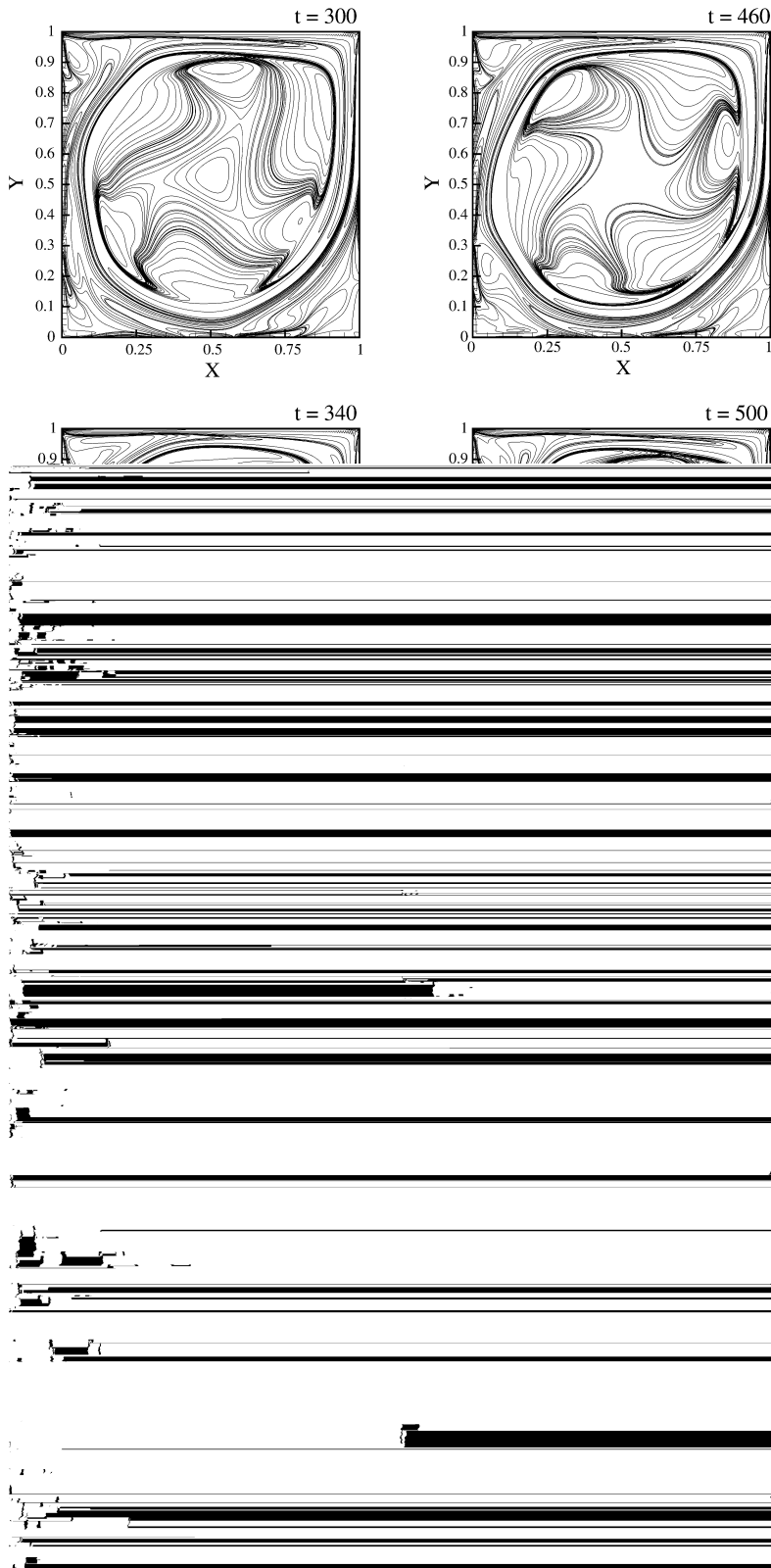
Fig. 4. Vorticity contours for the LDC problem obtained by CCD scheme for $Re = 10,000$ during $t = 300$ to $t = 580$ are shown. The vortical structures are stable. Identical contours are plotted in all the frames of Figs. 4 and 5.
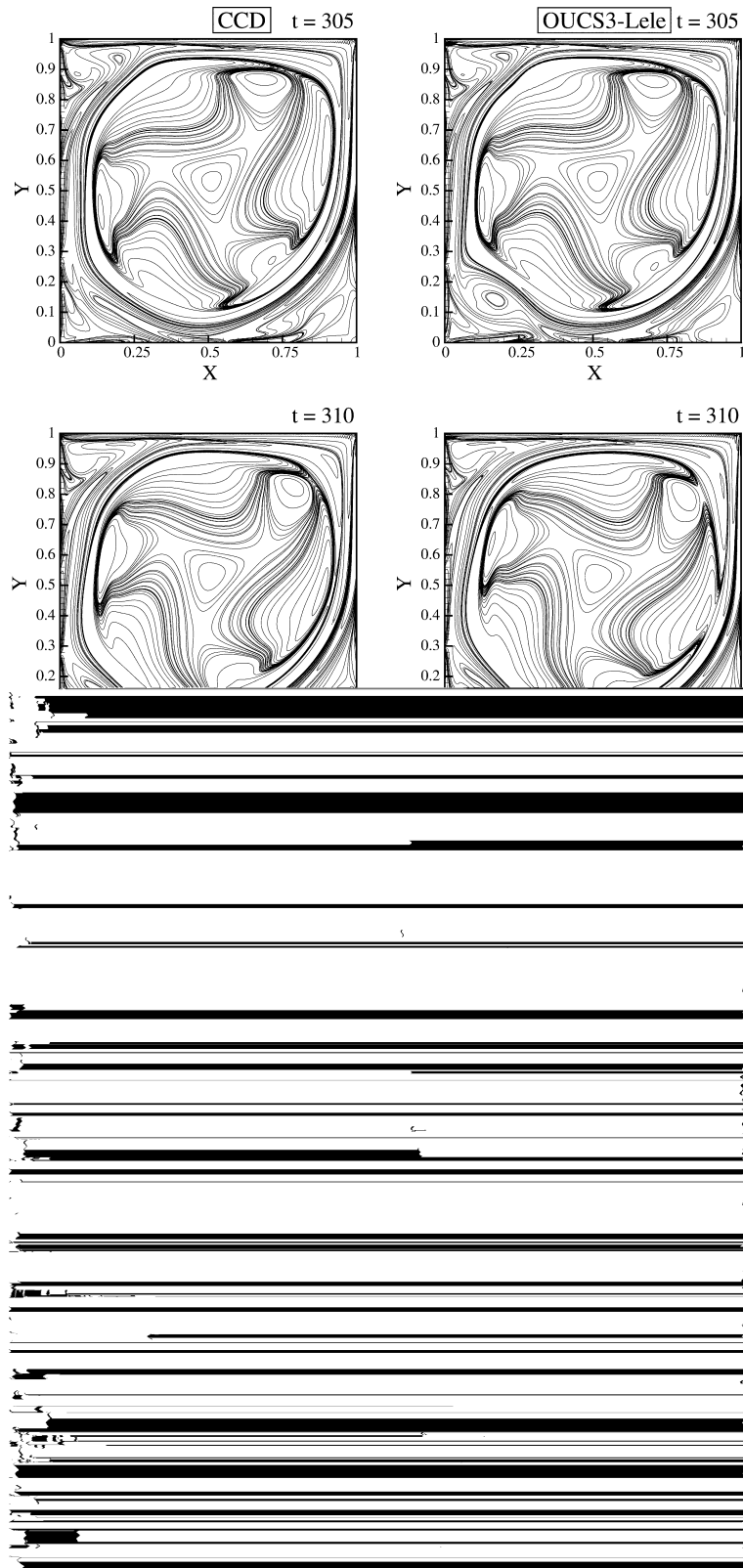
Fig. 5. Vorticity contours obtained using OUCS3–Lele method for $Re = 10,000$ during $t = 305$–$t = 340$, are compared with the solution obtained by CCD method. Solution at $t = 300$ is used as initial condition for the OUCS3–Lele method.
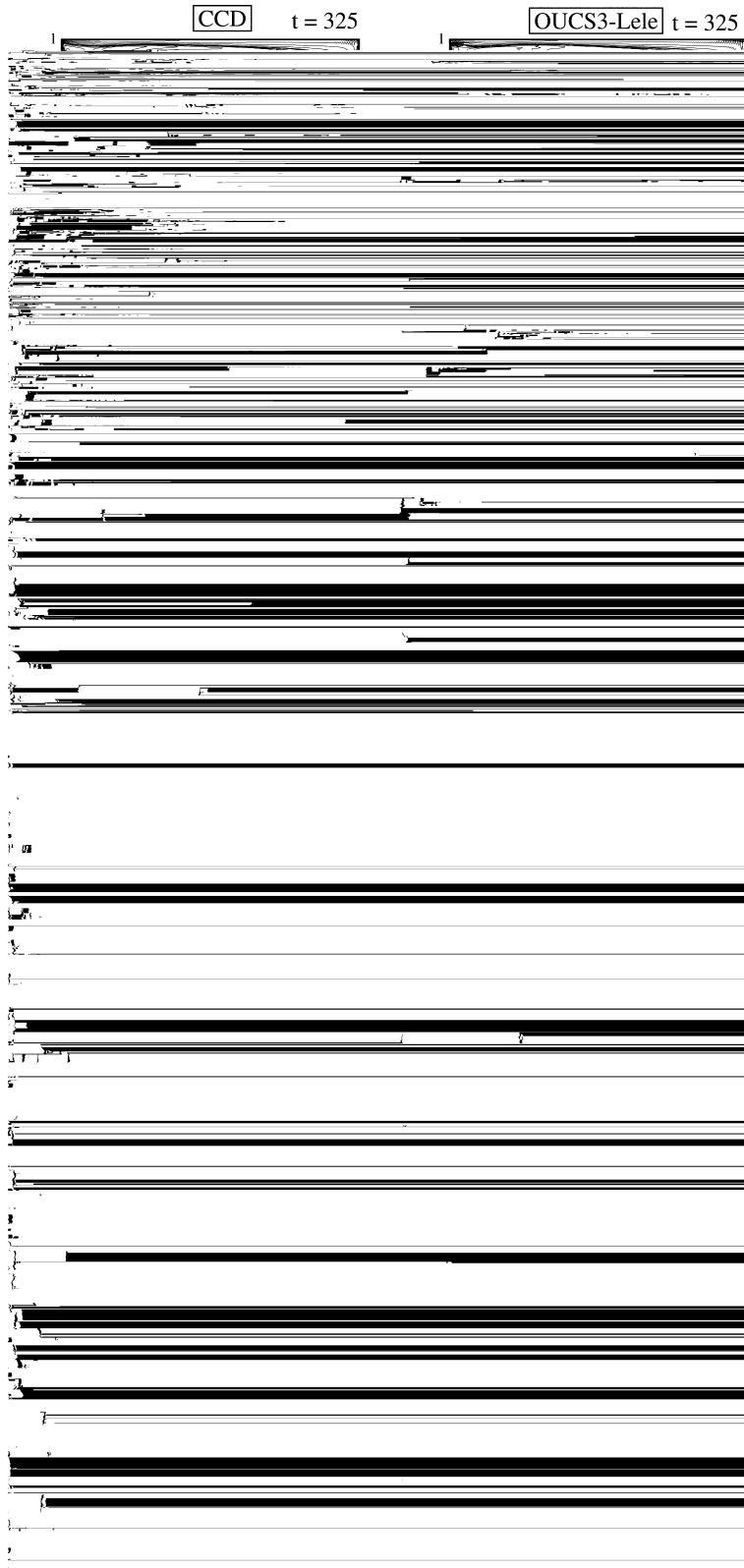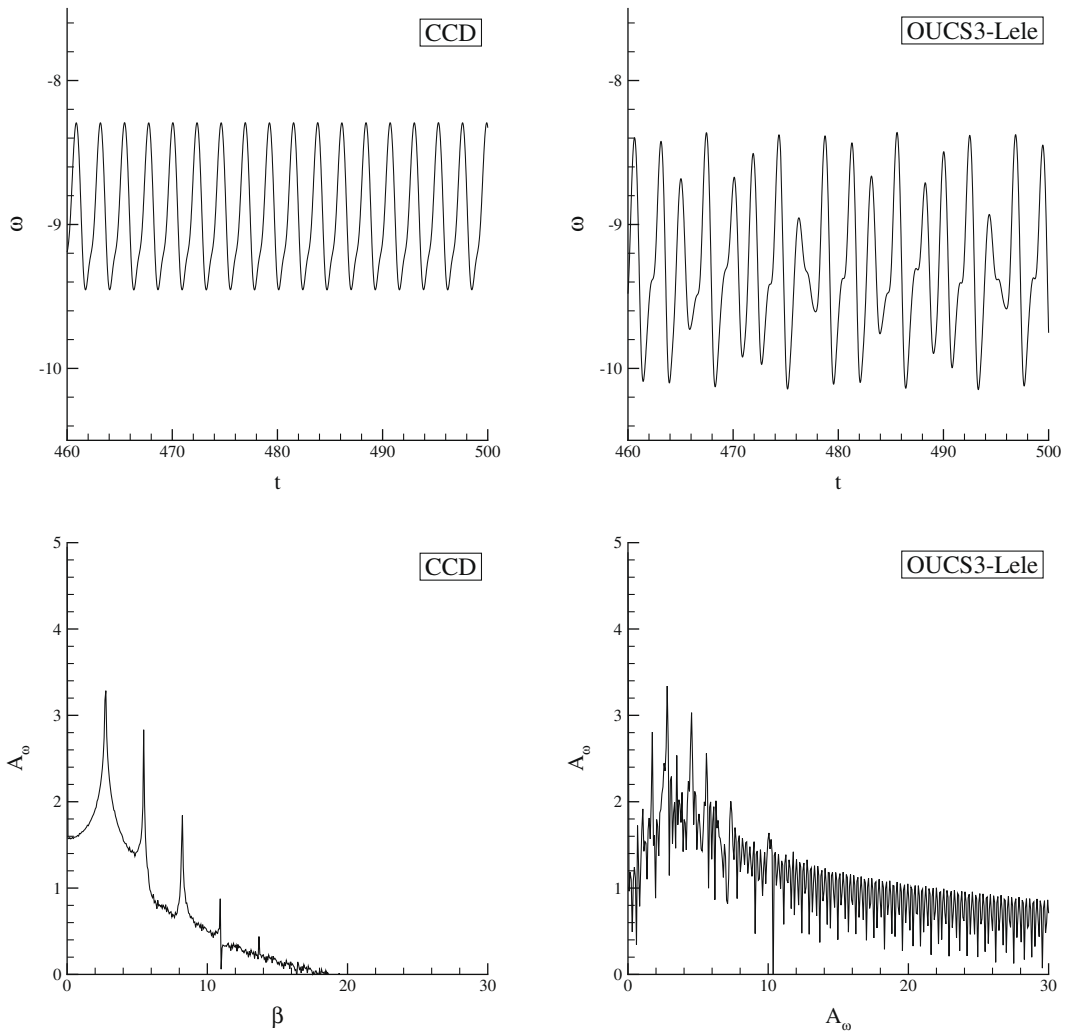
Fig. 5 (*continued*)

Fig. 6. The time history of vorticity at (0.95,0.95) obtained by CCD (top-left) and OUCS3–Lele (top-right) schemes. Corresponding frequency contents are shown in the bottom frames for these methods.

with the values reported in literature. The time history shows a time period of $t_p = 2.29$ for the CCD method and on an average $t_p = 2.30$ for the OUCS3–Lele methods. Also shown are the corresponding Fourier transforms of these signals immediately below the time histories. The left frame clearly shows the presence of distinct multiple modes occurring at frequencies $\beta = 2.73, 5.46, 8.22, 10.92, 13.68$ for the CCD method. However, in case of OUCS3–Lele method, there are no distinct modes and has wide spectrum which is directly due to larger aliasing effects due to poorer dissipation discretization. The most prominent peaks for this method are at $\beta = 1.738, 2.797, 3.476, 4.534, 5.59$ and shows them to be different from the peaks of CCD method and this is due to aliasing.

In order to further quantify aliasing error arising out of different computing methods, let us consider the product of two terms in the physical space given by,

$$q(x_j) = u(x_j)v(x_j) \tag{18}$$

Consider the finite Fourier series representation of the above terms in a uniform grid of size Δx. Thus, we have,

$$q(x_j) = \sum_{l=-\frac{N}{2}}^{\frac{N}{2}-1} Q_l e^{ik(j\Delta x)}$$

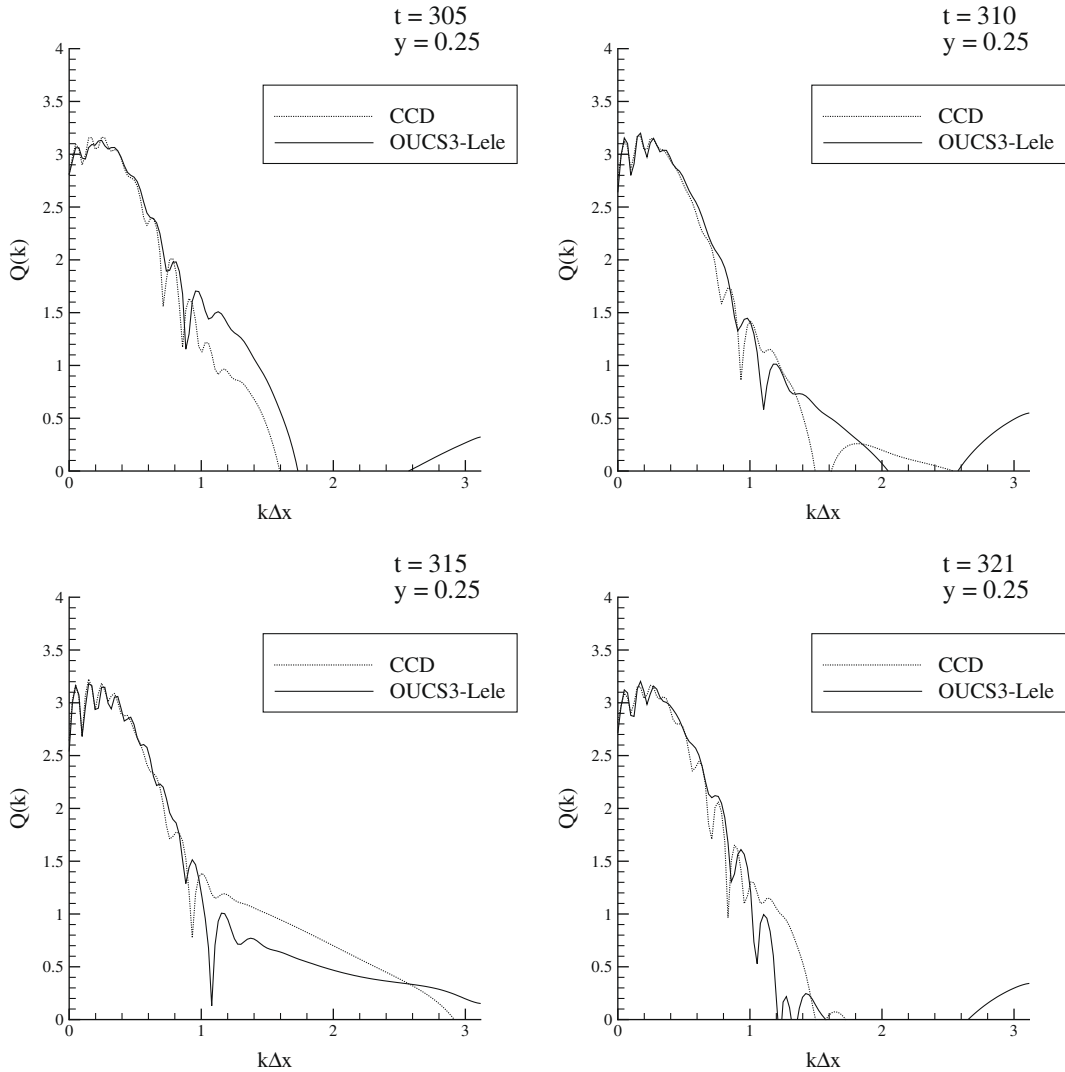$$u(x_j) = \sum_{n=-\frac{N}{2}}^{\frac{N}{2}-1} U_n e^{in(j\Delta x)}$$

Fig. 7. The Fourier amplitude of the product $q = \left(\frac{\partial \psi}{\partial y}\right)\left(\frac{\partial \omega}{\partial x}\right)$ is shown in spectral plane by plotting $Q(k)$ against $k\Delta x$ for the times shown in Fig. 5. The results of OUCS3–Lele method show higher aliasing as compared to CCD method.

$$v(x_j) = \sum_{m=-\frac{N}{2}}^{\frac{N}{2}-1} V_m e^{im(j\Delta x)}$$

where $\Delta x = \frac{2\pi}{N}$.

Forming the direct product and obtaining the Fourier transform of q, yields

$$Q_k = \sum_{n+m=k} U_n V_m + \sum_{n+m=k\pm N} U_n V_m \tag{19}$$

Note that the second term arises because the $(n+m)$ modes exceed the maximum resolved mode number N, i.e., the phase increases above $+\pi$ or goes below $-\pi$ (associated with $2\Delta x$ wavelength variation). In these cases, corresponding harmonics will have wavelengths corresponding to $[2\pi - (m+n)\Delta x]$, and will appear at a lower wave number. This phenomenon of *aliasing error* is visually noticeable as grid-scale oscillation for the largest resolved value of k.

In the following analysis with the Navier–Stokes solution, we consider one of the contributing products involved in the convection terms that create aliasing error: $q = u \frac{\partial \omega}{\partial x}$ where $u = \left(\frac{\partial \psi}{\partial y}\right)$. We evaluate this product from the computed solution in Figs. 4 and 5 at fixed specified height from the bottom at $y = 0.25$ of the computational domain at different times. In evaluating this product, we discretize the derivatives in the same combinations, as that is used in the actual computations: (a) CD_2 scheme for u and OUCS3 scheme for $\left(\frac{\partial \omega}{\partial x}\right)$ for the OUCS3–Lele method and (b) the CCD scheme for both u and $\left(\frac{\partial \omega}{\partial x}\right)$ for the CCD method. We represent the product q in it's correct Fourier–Laplace integral form as
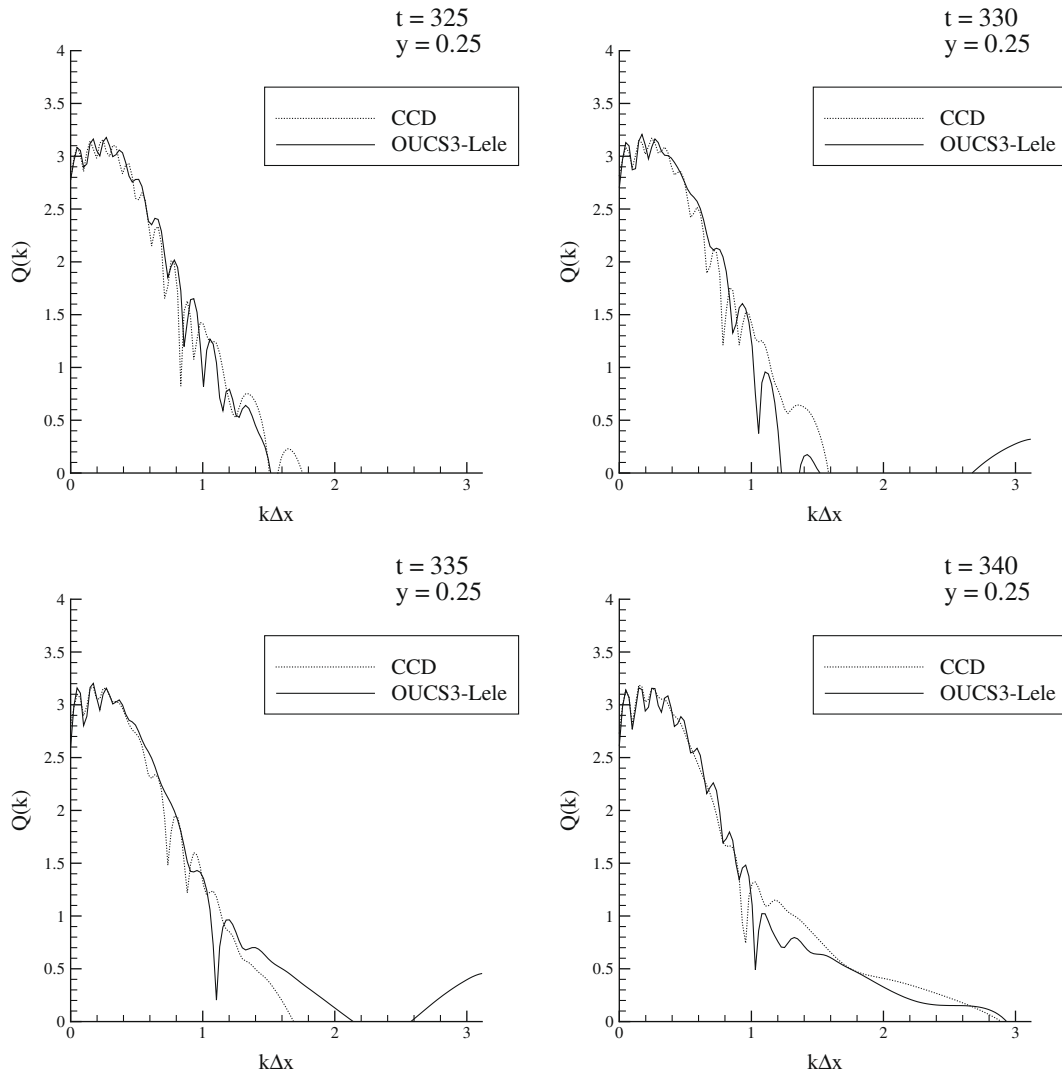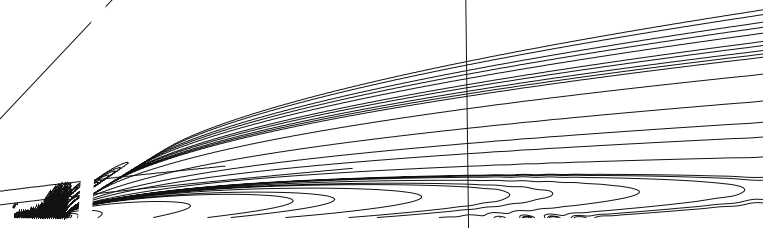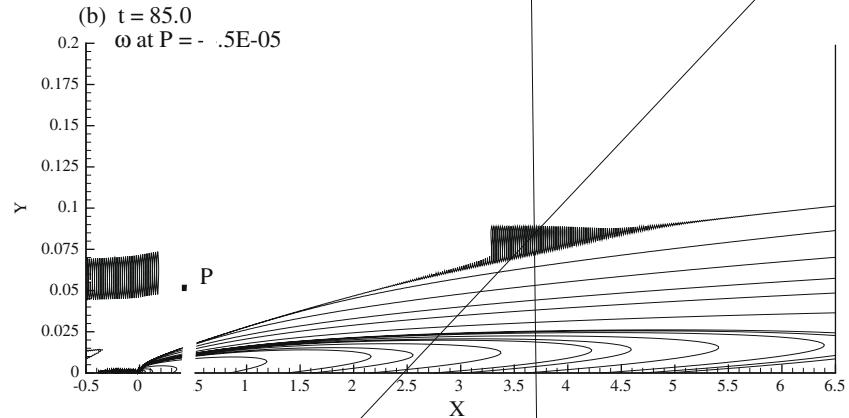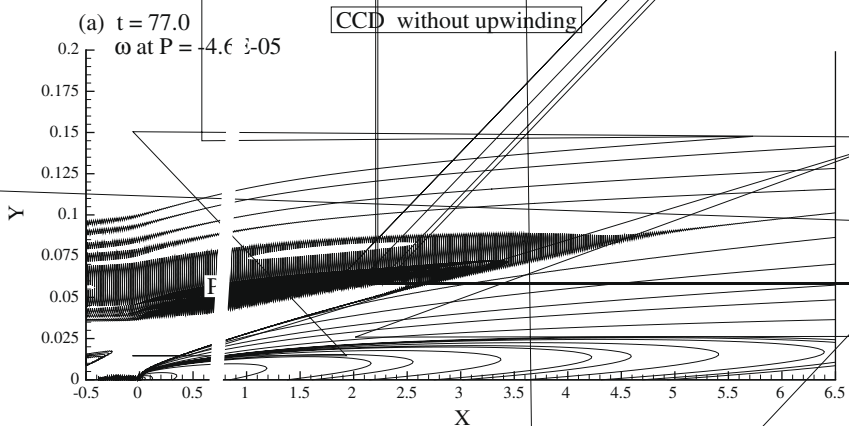
Fig. 7 (*continued*)

$$q(x,t) = \int_{-\infty}^{\infty} Q(k;t)e^{ikx}\,dk$$

The variation of $Q(k;t)$ are shown plotted in Fig. 7 at the indicated height and times. In all the figures, $Q(k)$ has higher value at higher wave numbers for the OUCS3–Lele method, as compared to the CCD method. Having a tail and non-zero value at the Nyquist limit in the spectrum provides an indication of aliasing error and it is clearly the case with the OUCS3–Lele method. Also, in the tail if the value of $Q(k;t)$ keeps increasing with k, then it is an indication of spurious energy pile-up that can lead to numerical instability due to aliasing. In both the methods, some small amount of aliasing effects are noted at times, but never high enough to cause instability or perceptible spurious oscillations. Due to added diffusion in CCD method at high k, this aliasing is controlled better at high k. From Fig. 7, it is clearly noted that the OUCS3–Lele method has a per-ceptible tail at all the time frames shown. Easy way to control the aliasing is by using more grid-points or using a very high-order filter to remove energy from the grid-scale level.

4. Receptivity calculation of adverse pressure gradient boundary layer flow

In the previous section, we have noted for an internal flow the CCD method to outperform another method that is a com-bination of two accurate compact schemes to evaluate first and second derivatives. We specifically noted the advantages of the CCD method which, while computing the second derivative reduces the problem of aliasing created by the convection

terms by over-emphasizing it at high k, that contributes to aliasing. In fact, aliasing accentuates due to higher accuracy of methods in calculating first derivatives. Lower order methods for calculating first derivative suppress this tendency due to band-limiting nature of the methods. These opposing effects of low and high accuracy methods are reversed when it comes to estimating second derivatives for the diffusion operator. In this case, lower accuracy methods under-emphasize dissipation while higher accuracy methods do just the opposite. The CCD method does even better at higher wave numbers, where it over-emphasizes dissipation counteracting the tendency of aliasing by the convection terms. Thus, we note that the CCD method works very well, when (i) we can use uniform grid and (ii) when the flow is strongly affected by dissipation terms everywhere in the flow, as is likely for internal vortex-dominated flows, as seen for the LDC problem.

(a) t = 77.0
ω at P = -4.6 E-05
CCD without upwinding

(b) t = 85.0
ω at P = - .5E-05

Fig. 9. Receptivity solution for the laminar flow shown in Fig. 8 to an excitation caused by a simultaneous blowing-suction strip at the wall for the indicated times is shown. The top frame result obtained by CCD method without upwinding that shows severe aliasing outside the shear layer. The bottom three frames show results obtained by CCD method with upwinding. Note the absence of aliasing in these frames.

inviscid part of the flow. This is further accentuated in the presence of adverse pressure gradient. Thus, lack of dissipation in that part of the flow, where large range of k are excited will continue to cause aliasing there. This is demonstrated here with the help of a flow forming over a flat plate experiencing adverse pressure gradient. For this flow, one can obtain a similarity profile by solving the Falkner–Skan equation [25]. However, such a similarity solution is valid only far away from the leading edge and for strong adverse pressure gradient the flow separates, invalidating thin shear layer approximation. Thus, the flow field is obtained by solving Navier–Stokes equation, including the leading edge of the plate so that the growth of the boundary layer is accounted for the receptivity calculation, when the flow is excited by a localized time-harmonic excitation source. This receptivity problem was experimentally and theoretically investigated in Seifert and Tumin [27] and its direct simulation results are presented here in 2D framework.

We have solved Navier–Stokes equation in two stages. Firstly, we solve it without any excitation, using the CCD method over the flat plate by taking (801×601) equispaced points in the stream-wise and wall-normal direction, respectively. The computational domain extends from $-0.5L \leqslant x \leqslant 7.5L$ in the stream-wise direction and $0 \leqslant y \leqslant 0.6L$, where L is the length scale of the problem and here it is fixed by the exciter location which is at a distance of $2.5L$ from the leading edge. Based on L, the computed flow is for $Re = 60,000$. The flow experiences an impressed adverse pressure gradient, given by the Falkner–Skan parameter, $m = -0.04762$, where $m = \frac{x}{U_e}\frac{dU_e}{dx}$ and U_e is the shear layer edge velocity. We apply a uniform flow condition at the inlet of the domain. On the top of the domain, a potential solution is used and at the outflow, a Sommerfeld type boundary condition is applied on the vorticity, as described in [28]. The equilibrium vorticity solution obtained by using the CCD method is depicted in Fig. 8 at $t = 77$ and $t = 85$, in the top two frames. The computational domain includes the leading edge of the plate, upstream of it there are no physical sources of dissipation. Thus, the flow experiences discrete jump in shear going along $y = 0$. The flow displays high frequency aliasing effects in the form of upstream propagating disturbances starting from the leading edge of the flat plate. These disturbances upon reflection from the inflow of the domain, attenuates while traveling downstream. Flow discontinuities also are seen to start from the edge of the shear layer that originates from the leading edge of the plate. These upstream propagating spurious disturbances are seen clearly in the top two frames of Fig. 8. If the problem is left unattended, this leads to solution divergence for the subsequent instability/ receptivity calculations, as shown in Fig. 9. Thus in the immediate neighborhood of the leading edge and above the shear layer, flow is inviscid but experiences sharp gradient that works as a site from where aliasing error is trigerred. In the middle frame of Fig. 8, solution is shown at $t = 85$ and one can see undiminished problem in the computed flow field. Specifically, a point P is identified where the level of spurious vorticity value is of the order of 10^{-5} that persists for the CCD method in calculating the laminar equilibrium flow.

Reason for the persistence of aliasing error created is due to the fact that the CCD scheme is central in nature. One of the ways to tackle this problem is to use upwinding in evaluating the convection terms. In performing this, we add explicitly a fourth-order dissipative term to the calculated first derivative, that is of the type $\eta \Delta x^3 \frac{\partial^4 \omega}{\partial x^4}$ for the stream-wise derivative. Here, one chooses η as a user-defined constant to control the quantity of upwinding. A similar term is added to the y-derivative of the vorticity. As the CCD method has excellent dissipation discretization property, one does not, in general, require to add large explicit higher order dissipation inside the shear layer. This observation is used in fixing the dissipative constant η. In the wall-normal direction, η is chosen as 0.08 for all heights. In the bottom frame of Fig. 8, results are shown for the equilibrium solution obtained using this upwinded CCD method at $t = 105$. This upwinding is applied using the solution at $t = 77$. One can clearly see the total absence of aliasing outside the shear layer. It is noted that the value of ω is zero at the designated point P.

In Fig. 8, it is shown how one can further improve the CCD method proposed in [4] in controlling aliasing error for high accuracy calculations of a shear and pressure driven equilibrium flow. More intricate requirements from the numerical method are needed, when it is used to solve for higher order quantities. In the present exercise, we are looking for the receptivity solution for disturbance quantities by solving Navier–Stokes equation for the equilibrium and the disturbance flows. The equilibrium solution shown in Fig. 8 is perturbed by a time-harmonic localized source at the wall. It is well known that boundary layers respond to such excitations by displaying spatially growing waves caused by the instability of the laminar equilibrium flow, if the excitation frequency is neither too low or too high. Here, a simultaneous blowing-suction type harmonic exciter is used that creates a normal velocity perturbation given by, $v_d = A_m \sin(6.546t)$, where the amplitude of the perturbation is given by, $A_m = (-15.1875\xi^5 + 35.4375\xi^4 - 20.25\xi^3)$. The non-dimensional variable is defined via, $\xi = \frac{(x-2.48)}{0.02}$. This type of excitation field was also used in [28].

Typical solutions to this receptivity problem are demonstrated in Fig. 9 for the above excitation at the indicated time instants. In the top frame, the solution obtained by the CCD method without any upwinding is shown. One notes the computed flow field to be contaminated severely by aliasing error – outside and within the shear layer. Outside the shear layer it originates from the discontinuity line starting from the leading edge of the plate and inside the shear layer, it is noted near the outflow. The level of error seen at $t = 11$ is two orders of magnitude larger than that was noted for the equilibrium flow at the same designated point, P. The excitation was applied to the solution at $t = 77$ shown in Fig. 8 and the time counter is advanced from zero. Thus, the solution indicates severe degradation with time. In fact the solution shown in the top frame was numerically destabilized, a few time steps later. Another set of calculations are performed starting from the same initial data with the same upwinding used for the equilibrium solution of Navier–Stokes equation. The computed solutions are shown in the bottom three frames of Fig. 9. Significant improvement of results are seen in all the three frames, despite the fact that the equilibrium solution was itself contaminated. At the designated point P, the induced vorticity value reduces to zero. Also, the aliasing error reduces inside the shear layer, near the outflow of the computational domain.

5. Conclusion

Here the CCD scheme recently proposed in [4], has been further analyzed and modifications suggested in solving Navier–Stokes equation for an internal and an external flow. The CCD scheme is known for its better dissipation discretization properties as compared to any other explicit and implicit schemes. We have additionally defined a gain and a loss function to quantify the effectiveness of dissipation discretization and various methods have been compared in Figs. 2 and 3. It is noted that followed by CCD method, the OUCS3 method applied twice seemed to perform well. In [4] the DRP properties were shown for the CCD method in solving wave propagation problems. Here, we study the aliasing error property of CCD method in comparison to some other compact schemes. It is shown that the better de-aliasing property of CCD method is actually related to its dissipation discretization property.

The above properties were investigated with respect to benchmark internal and external flows. The square lid-driven cavity problem at $Re = 10,000$ is investigated to show the existence of a new "equilibrium solution", whose existence is related to better resolution and de-aliasing property of the present scheme. However, when the same method is used to study the receptivity of a boundary layer by solving the Navier–Stokes equation, it was found that problems occurred outside the thin shear layer in the form of aliasing. By solving additionally the receptivity to time-harmonic localized excitation on the surface, we noted that modifications, in terms of upwinding the convection terms are required. This aspect of CCD scheme was not known before and the present solution seems to work extremely well in solving this problem of flow instability and receptivity.

References

[1] R. Peyret, T.D. Taylor, Computational Methods for Fluid Flow, Springer Verlag, New York, 1983.
[2] P.C. Chu, C. Fan, A three-point combined compact difference scheme, J. Comput. Phys. 140 (1998) 370–399.
[3] Q. Zhou, Z. Yao, F. He, M.Y. Shen, A new family of high-order compact upwind difference schemes with good spectral resolution, J. Comput. Phys. 227 (2) (2007) 1306–1339.
[4] T.K. Sengupta, V. Lakshmanan, V.V.S.N. Vijay, A new combined stable and dispersion relation preserving compact scheme for non-periodic problems, J. Comput. Phys. 228 (8) (2009) 3048–3071.
[5] S.K. Lele, Compact finite difference schemes with spectral-like resolution, J. Comput. Phys. 103 (1992) 16–42.
[6] T.K. Sengupta, G. Ganeriwal, S. De, Analysis of central and upwind schemes, J. Comput. Phys. 192 (2) (2003) 677–694.
[7] T.K. Sengupta, S.K. Sircar, A. Dipankar, High accuracy schemes for DNS and acoustics, J. Sci. Comput. 26 (2) (2006) 151–193.
[8] K. Mahesh, A family of high-order finite difference schemes with good spectral resolution, J. Comput. Phys. 145 (1998) 332.
[9] R. Vichnevetsky, J.B. Bowles, Fourier analysis of numerical approximations of hyperbolic equations, SIAM Stud. Appl. Math., vol. 5, SIAM, Philadelphia, USA, 1982.
[10] L.N. Trefethen, Group velocity in finite difference schemes, SIAM Rev. 24 (2) (1982) 113–136.
[11] T.K. Sengupta, A. Dipankar, P. Sagaut, Error dynamics: beyond von Neumann analysis, J. Comput. Phys. 226 (2007) 1211–1218.
[12] G.F. Carnevale, R.C. Kloosterziel, Emergence and evolution of triangular vortices, J. Fluid Mech. 259 (1994) 305–331.
[13] M. Beckers, G.J.F. van Heijst, The observation of a traingular vortex in a rotating fluid, Fluid Dyn. Res. 22 (1998) 265–279.
[14] T.K. Sengupta, Fundamentals of Computational Fluid Dynamics, Universities Press, Hyderabad, India, 2004.
[15] A. Arakawa, Computational design of long term numerical integration of the equations of fluid motion: two-dimensional incompressible flow, J. Comput. Phys. 1 (1966) 119–143.
[16] R.M. Kirby, G.Em. Karniadakis, De-aliasing on non-uniform grids: algorithms and application, J. Comput. Phys. 191 (1) (2003) 249–264.
[17] N. Park, J.Y. Yoo, H. Choi, Discretization errors in large eddy simulation: on the suitability of centered and upwind-biased compact differencing scheme, J. Comput. Phys. 198 (2004) 580–616.
[18] C.A. Kennedy, A. Gruber, Reduced aliasing formulations of the convective terms within the Navier–Stokes equations for a compressible fluid, J. Comput. Phys. 227 (3) (2008) 1676–1700.
[19] C. Canuto, M.Y. Hussaini, A. Quarteroni, T.A. Zang, Spectral Methods in Fluid Dynamics, Springer Verlag, New York, USA, 1988.
[20] H.K. Moffatt, Viscous and resistive eddies near a sharp corner, J. Fluid Mech. 18 (1964) 1–18.
[21] C.-H. Bruneau, M. Saad, The 2D lid-driven cavity problem revisited, Comput. Fluids 35 (2006) 326–348.
[22] F.H. Harlow, C.H. Welch, Numerical calculation of time-dependent viscous incompressible flow of fluid with free surface, Phys. Fluids 8 (21) (1965) 82–98.
[23] Y.-F. Peng, Y.-H. Shiau, R.R. Hwang, Transition in a 2D lid driven cavity flow, Comput. Fluids 32 (2003) 337–352.
[24] H.A. Van Der Vorst, Bi-CGSTAB: a fast and smoothly converging variant of Bi-CG for the solution of nonsymmetric linear systems, SIAM J. Sic. Stat. Comput. 13 (2) (1992) 631–644.
[25] T. Cebeci, P. Bradshaw, Momentum Transfer in Boundary Layers, Hemisphere Publishing Corporation, USA, 1977.
[26] T.K. Sengupta, M.T. Nair, Upwind schemes and large eddy simulation, Int. J. Numer. Meth. Fluids 31 (1999) 879–889.
[27] A. Seifert, A. Tumin, Nonlinear localized distrubances in an adverse pressure gradient boundary-layer transition: experiment and linear stability analysis, in: P. Zarachan (Ed.), Prog. in Fluid Flow Research: Turbulence and Applied MHD, vol. 182, Progress in Astronautics and Aeronautics series, 1998.
[28] K. Venkatasubbaiah, T.K. Sengupta, Mixed convection flow past a vertical plate: stability analysis and its direct simulation, Int. J. Therm. Sci. 48 (3) (2009) 461–474.